AIAA 90 – 0080

DEVELOPMENT OF THE UTA HYPERSONIC SHOCK TUNNEL

W. S. Stuessy, R. G. Murtugudde, F. K. Lu, and D. R. Wilson
The University of Texas at Arlington
Arlington, Texas 76019

28th Aerospace Sciences Meeting
January 8-11, 1990/Reno, Nevada

DEVELOPMENT OF THE UTA HYPERSONIC SHOCK TUNNEL

W. S. Stuessy,[+] R. G. Murtugudde,[+] F. K. Lu,[*] and
D. R. Wilson[**]
The University of Texas at Arlington
Arlington, Texas 76019

Abstract

The development of a new hypersonic shock tunnel facility at the Aerodynamics Research Center of The University of Texas at Arlington is described in this paper. The shock tunnel employs a 400 atm (6000 psi) helium-air shock tube driver operated in the reflected mode, and is capable of simulating hypersonic flight at Mach numbers ranging from 5 to 16. The operational theory, test facility development and estimated facility performance are presented, together with test results from the initial facility calibration at Mach 8.

Nomenclature

A	Area	u	Flow velocity
a	Speed of sound	X	Driven tube length
M	Mach number	x	Distance
P	Pressure	α	$\gamma+1/\gamma-1$
t	Time	β	$\gamma-1/2\gamma$
U	Wave velocity	γ	Specific heat ratio

Subscripts

cs	Contact surface	r	Reflected shock wave
D	Driven tube	s	Incident shock wave
e	Equilibrium	t	Nozzle throat
N	Nozzle	0	Stagnation conditions
DW	Disturbance wave	1-8	Refer to Fig. 2

Superscript

*	Sonic condition	′	Transmitted condition

Introduction

The basic shock tube has been exploited as a practical research facility for over half a century. The shock tube has been widely used for the study of chemical and physical problems associated with high-speed flow,[1-3] and for basic investigations of the structure of shock waves and the kinetics of chemical reactions.[4]

The Mach number simulation capability of a shock tube is limited to supersonic speeds, but hypersonic Mach numbers can be generated by adding an acceleration nozzle to the end of the shock tube. Hertzberg[5] originally suggested this modification, which is referred to as a 'Shock Tunnel'. Two basic types of shock tunnels are currently in use: the non-reflected tunnel, in which the flow behind the incident shock wave is expanded directly through a diverging nozzle attached to the end of the driven tube; and the reflected tunnel, which uses a secondary diaphragm to reflect the incident shock wave from the end of the driven tube and stagnate the gas flow prior to expansion through a converging-diverging nozzle. The relative merits of each type are discussed in the following section. Both types have been widely used, and recent surveys of the operational status and performance capabilities of various hypersonic shock tunnels are presented in Refs. 6-7.

The hypersonic shock tunnel constructed at The University of Texas at Arlington (UTA) Aerodynamics Research Center (ARC) was based on the reflected shock wave concept. Figure 1 shows the layout of the UTA shock tunnel. A brief review of the preliminary design considerations, theory of operation and tunnel starting analysis is given in the following section. This is followed by an estimate of the test facility performance capabilities, and presentation of experimental results from the initial operation of the tunnel at Mach 8. The facility development is described in greater detail in Refs. 8-10.

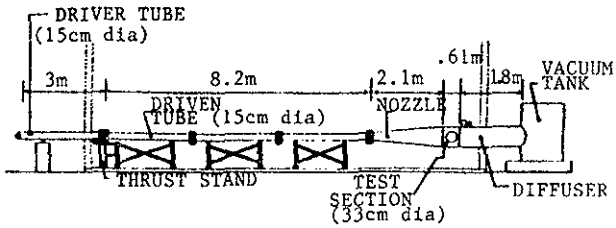

Fig. 1. UTA Hypersonic Shock Tunnel

Design Considerations

Selection of Operating Mode

As mentioned in the Introduction, two basic types of shock tunnels are currently in use. A non-reflected tunnel expands the flow behind the incident shock wave directly through the nozzle and into the test section. The nozzle entrance has the same area as the driven tube in this tunnel design. The passage of the incident shock and its associated wave system through the nozzle initiates the flow. Uniform flow is terminated by the arrival of the contact surface in the test section. The total pressure in the test section is limited to the pressure behind the incident shock wave. The boundary layer in this type of tunnel is usually larger than in a reflected tunnel and can be so large that a method of reducing it must be used in many cases.

[+] Graduate Research Associate, Student Member AIAA
[*] Assistant Professor of Aerospace Engineering, Member AIAA
[**] Professor of Aerospace Engineering, Associate Fellow AIAA

The non-reflected tunnel is characterized by very short test times.

A reflected tunnel uses a secondary diaphragm at the end of the driven tube to reflect the incident shock wave. The reflected shock wave increases the stagnation enthalpy to a higher level and allows the gas to be expanded to higher test section Mach numbers than for a non-reflected tunnel. The high pressure behind the reflected shock wave ruptures the secondary diaphragm and initiates the flow through the nozzle and test section. The reflected tunnel generally has longer available testing time than the non-reflected tunnel.

Although a non-reflected tunnel has certain advantages from the standpoint of being able to more closely maintain equilibrium flow in the subsequent nozzle expansion, the double advantages of the longer test time and higher total enthalpy simulation capability of the reflected mode of operation led to its selection as the basic operating concept for the UTA shock tunnel.

Theory of Operation (Reflected Mode)

The basic operation of the reflected-mode hypersonic shock tunnel is illustrated by the wave diagram shown in Fig. 2. The driver tube is pressurized

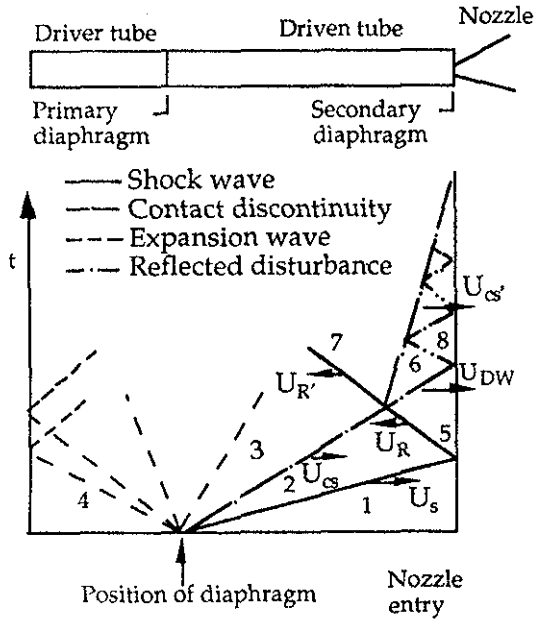

Fig. 2. Wave Diaphragm for a Reflected Shock Tunnel

to the desired pressure level using a gas booster pump. A double-diaphragm section is pressurized along with the driver tube but at about half the pressure of the driver pressure so that the pressure differential across each of the two diaphragms is approximately the same. Vacuum pumps are used to set the initial pressure levels in the driven tube and the nozzle, test section, and diffuser. After all pressure levels are at their desired values, the tunnel is started by opening a vent valve in the primary diaphragm region. When the pressure drops sufficiently in the diaphragm section, the upstream diaphragm will rupture due to the large pressure differential. This loads the downstream diaphragm, which quickly ruptures to start operation of the tunnel.

The rupture of the primary diaphragms initiates the formation of a shock wave which travels down the driven tube and an expansion wave that moves upstream into the driver tube. The head of the expansion wave travels into the driver tube at the local speed of sound,

$$\frac{dx}{dt} = -a_4 \tag{1}$$

The tail of the expansion fan will also propagate at the speed of sound relative to the local flow

$$\frac{dx}{dt} = u_3 - a_3 \tag{2}$$

and may travel either upstream or downstream depending upon the velocity behind the incident shock wave.

The incident shock wave is followed by another discontinuity, the contact surface, which propagates down the driven tube at a velocity equal to the gas velocity behind the incident shock wave (u_2). The pressure and gas velocity are unchanged across the contact surface but the temperature, density, and entropy all change across the contact surface.

For developing the preliminary design concept, the shock tube was analyzed using perfect gas relations.[11,12] With these assumptions, the incident shock velocity can be calculated from the initial conditions of the driver and driven gas. An iteration scheme is used to calculate the pressure ratio P_2/P_1 across the incident shock from the initial pressure ratio P_4/P_1

$$\frac{P_4}{P_1} = \frac{P_2}{P_1}\left\{1 - \frac{(\gamma_4 - 1)(a_1/a_4)(P_2/P_1 - 1)}{\sqrt{2\gamma_1\left[2\gamma_1 + (\gamma_1 + 1)(P_2/P_1 - 1)\right]}}\right\}^{\frac{-2\gamma_4}{\gamma_4 - 1}} \tag{3}$$

and then the shock velocity U_s can be calculated from

$$U_s = M_s\, a_1 \tag{4}$$

where

$$M_s = \sqrt{1 + \frac{\gamma - 1}{2}\left(\frac{P_2}{P_1} - 1\right)} \tag{5}$$

The incident shock is reflected if the end of the shock tube is effectively closed. This requirement can be met by insuring that the nozzle throat-to-driven tube diameter ratio is sufficiently small, or by the use of a secondary diaphragm at the end of the shock tube. If the nozzle entry is sufficiently small, the gas flow

velocity u_5 is zero, and under these conditions, the pressure ratio across the reflected shock can be written as[4]

$$P_{52} = P_{53} = \frac{P_{21}(\alpha+2) - 1}{P_{21} + \alpha} \tag{6}$$

where $\alpha = \gamma + 1/\gamma - 1$. The velocity U_R of the reflected shock is given by

$$\frac{U_R}{U_s} = -\frac{(\alpha-1) + 2P_{21}}{1 + \alpha P_{21}} \tag{7}$$

and the speed of sound ratio is given by

$$a_{52}^2 = \frac{P_{52}(P_{52} + \alpha - 1)}{\alpha P_{52} + 1} \tag{8}$$

When the interaction of the reflected shock with the contact surface occurs, there will in general be a reflected disturbance wave as well as the transmitted shock wave and contact surface. However, after the interaction, the equality of the static pressure and velocity on both sides of the transmitted contact surface must still be satisfied. With the notation of Fig. 2, these can be stated as $P_6 = P_7$ and $u_6 = u_7$. The velocity change across the transmitted shock can be written as

$$\frac{u_3 - u_7}{a_3} = \sqrt{\frac{2}{\gamma(\gamma-1)}}\ \frac{(P_{73} - 1)}{(\alpha P_{73} + 1)^{1/2}} \tag{9}$$

For a disturbance reflected as a shock, the velocity ratio can be written as

$$\frac{u_6 - u_5}{a_5} = \sqrt{\frac{2}{\gamma(\gamma-1)}}\ \frac{(P_{65} - 1)}{(\alpha P_{65} + 1)^{1/2}} \tag{10}$$

But by our assumption $u_5 = 0$. The velocity change in the case of an expansion wave disturbance reflection would be

$$\frac{u_6}{a_5} = -\frac{(1 - P_{65}^{\beta})}{\gamma\beta} \tag{11}$$

where $\beta = \gamma - 1/2\gamma$.

The specific heat ratio is represented by γ for both the driver and driven gases in all the above equations. However, if the driver and driven gases have different ratios then γ_4 and γ_1 can be used to denote the specific heat ratios of the driver and driven gas respectively. Now, equating the velocities across the contact surface ($u_6 = u_7$), we get the following relations from Eqs. 9-11.

$$\sqrt{\frac{2}{\gamma_4(\gamma_4 - 1)}}\ \frac{(P_{73} - 1)}{(\alpha_4 P_{73} + 1)^{1/2}} = \frac{u_3}{a_3} - a_5 \sqrt{\frac{2}{\gamma_1(\gamma_1 - 1)}}\ \frac{(P_{65} - 1)}{(\alpha_1 P_{65} + 1)^{1/2}} \tag{12}$$

for a reflected shock disturbance, and

$$\sqrt{\frac{2}{\gamma_4(\gamma_4 - 1)}}\ \frac{(P_{73} - 1)}{(\alpha_4 P_{73} + 1)^{1/2}} = \frac{u_3}{a_3} + \frac{a_5(1 - P_{65}\,\beta_1)}{a_3\,\gamma_1\,\beta_1} \tag{13}$$

for a reflected expansion wave disturbance. The velocity of the reflected shock disturbance, U_{DW}, can be written as

$$\frac{U_{DW}}{a_5} = \{\beta_1\,(\alpha_1 P_{65} + 1)\}^{1/2} \tag{14}$$

The reflected expansion wave disturbance travels at the speed of sound a_5.

If the conditions on either side of the contact surface are such that the reflection from the contact surface - reflected shock intersection is a Mach wave, then the pressure ratio $P_{65} = 1$. This is the tailored-interface condition[13] and the incident shock Mach number for which this condition occurs is the tailoring Mach number. Hence, the pressure ratio across the transmitted shock wave becomes equal to the pressure ratio across the shock reflected from the end of the shock tube, that is

$$P_{73} = P_{52} \tag{15}$$

because $P_3 = P_2$ across the contact surface. Now Eqs. 12 and 13 reduce to

$$\frac{u_3}{a_3} = \sqrt{\frac{2}{\gamma_4(\gamma_4 - 1)}}\ \frac{(P_{52} - 1)}{(\alpha_4 P_{52} + 1)^{1/2}} \tag{16}$$

These equations can be solved for the incident shock Mach number, which, for the given initial conditions in the shock tube satisfies the tailoring condition. These calculations were performed for both a constant area shock tube and for a shock tube with an area reduction at the primary diaphragm,[8] and the results are presented in Figs. 3-6. The tailored-interface condition is illustrated in Fig. 3. The variation of the required driver temperature T_4 is shown in Fig. 4. As the initial driver temperature increases, the tailoring Mach number also increases. Of course, operation in the tailored-interface mode will require a heater mechanism for the driver tube.

The calculated pressure ratios are shown in Figures 5 and 6. The pressure ratio across the disturbance reflection, P_{85}, is given by

$$P_{85} = \frac{P_{65}(\alpha_1 + 2) - 1}{P_{65} + \alpha_1} P_{65} \tag{17}$$

for reflected shock wave disturbance, and by

$$P_{85} = \left(2P_{65}^{\beta_1 - 1}\right)^{1/\beta_1} \tag{18}$$

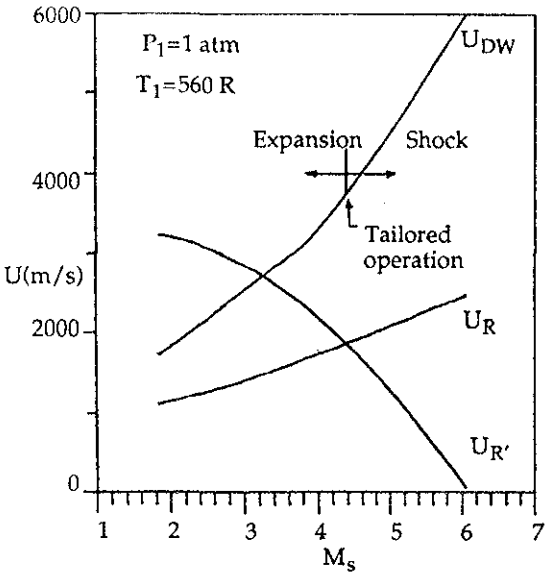

Fig. 3. Velocities of the Waves Reflected and Transmitted by the Contact Surface

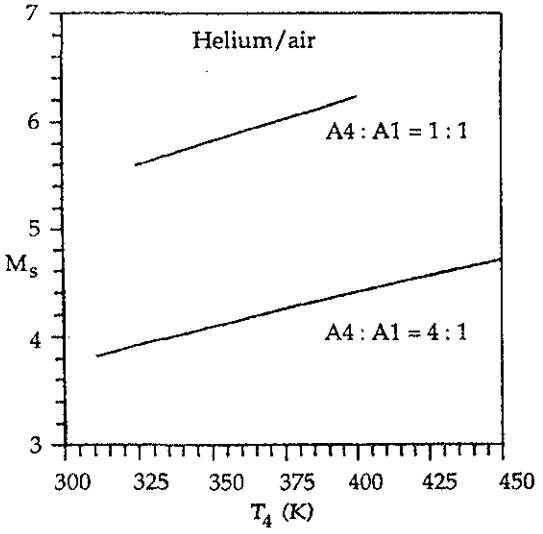

Fig. 4. Variation of Tailoring Shock Mach Number with Initial Driver Temperature

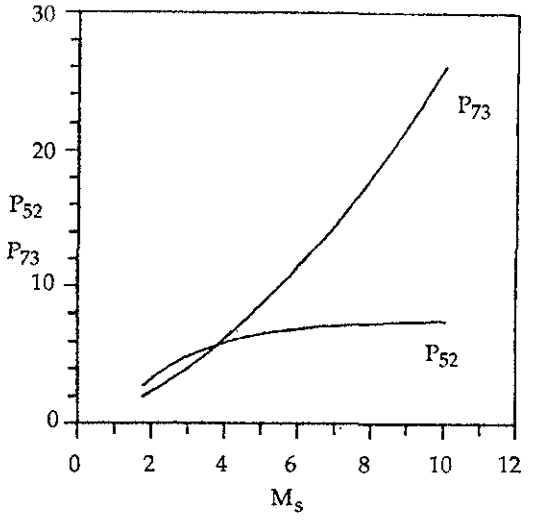

Fig. 5. Pressure Ratio across the Reflected Shock Wave

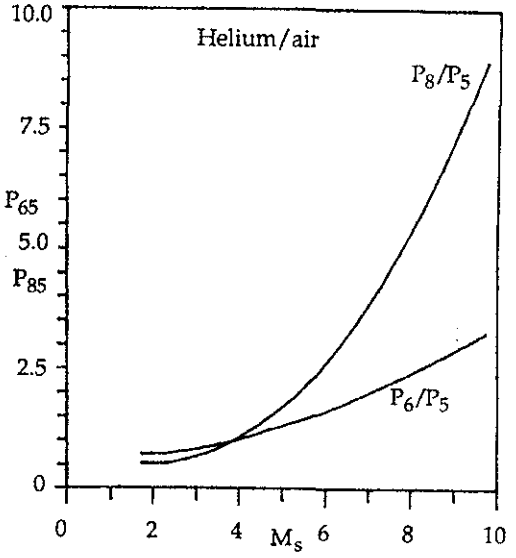

Fig. 6. Pressure Ratio across the Reflected Disturbance from the Contact-Surface-Reflected Shock Interaction

for an expansion wave reflected from the contact surface. The disturbance reflected as an expansion wave from the contact surface-reflected shock interaction corresponds to pressure ratios less than one. And, P_{85} is less than P_{65} in this range of shock Mach numbers because the gas in region 8 is expanded from region 6. The reflected shock disturbance compresses the gas from region 6, and hence P_{85} is higher than P_{65}. The shock Mach number for which the pressure ratios are equal to unity corresponds to a disturbance which is a Mach wave. Hence this shock Mach number is the tailoring Mach number. The rapid increase in the pressure in region 8 is critical for the design pressure rating of the driven tube. P_8, rather than P_5, should be considered for design. It is not always possible to operate at exactly the tailoring Mach number. So, if the reflected tunnel is operated at higher than tailoring Mach numbers, then these high pressures could be reached.

The contact surface will be brought substantially to rest by the multiple wave reflections between the end wall and the contact surface. However, since it is not practically possible to attain the tailoring Mach number for all operational conditions of the tunnel, the advantage of the reflected mode tunnel in terms of higher test times than attainable with the nonreflected

mode is greatly reduced. The 'Equilibrium' operating mode[14] can be used to overcome this difficulty. In the equilibrium mode the effect of the disturbances subsequent to the first reflected disturbance from the contact surface is assumed to be negligible. This is equivalent to assuming that the contact surface is brought to rest by the first transmitted shock. The expression for equilibrium can be now written as

$$\sqrt{\frac{2}{\gamma_4(\gamma_4-1)}}\ \frac{(P_{e3}-1)}{(\alpha_4 P_{e3}+1)^{1/2}} = \frac{u_3}{a_3} \qquad (19)$$

The pressures calculated from the above relation are compared with the pressure ratio, P_8, in Fig. 7. The pressure P_8 is within 10 percent of the equilibrium pressure for a wide range of shock Mach numbers. This suggests that the flow after the arrival of the first disturbance from the contact surface can be used to supply the nozzle to achieve the advantages of tailored operation over a wider range of shock Mach numbers. Moreover, the flow before the first disturbance can be used for the nozzle starting process; that is to establish steady flow in the test section. The duration of uniform flow in the test section is one of the important design factors for a shock tunnel.

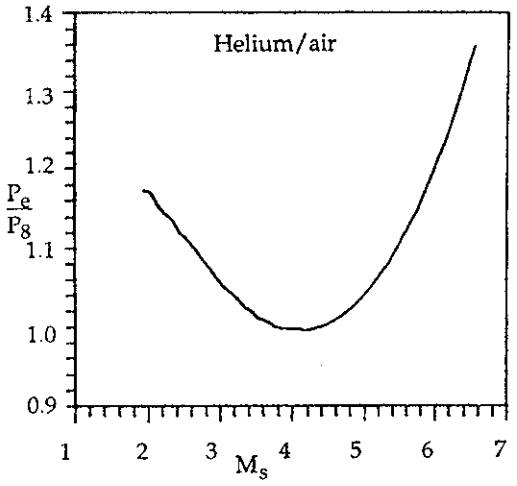

Fig. 7. Variation of Equilibrium Pressure Ratio

Steady Flow Duration

A detailed analysis of the steady flow duration for the test section flow was performed in Ref. 8. This analysis considered the effects (1) theoretical test times for operation in the tailored-interface mode, (2) reductions in test time associated with operation in the "equilibrium" mode,[14] (3) reductions in test time associated with arrival of the head and/or tail of the driver tube expansion wave, and (4) time required to establish steady flow in the nozzle expansion.[14,15] The results of this analysis indicated that test section steady flow periods of 3-5 msec could be expected for a wide range of tunnel operating conditions.

Shock Tube Boundary Layer Effects

The previous analysis has been based on an inviscid flow assumption, however the real flow in the shock tube will be influenced by the boundary layer growth in the flow induced by the incident shock wave. A study of shock attenuation due to boundary layer growth was conducted by Huang [17] using the classical shock tube boundary layer theory of Mirels[18]. The results of this study showed that the primary effect is an increase in the required value of P_4/P_1 to get the same shock Mach number. Thus by using measured values of M_s near the end of the driven tube rather than inviscid calculations of M_s as a function of P_4/P_1, the conclusions of the previous analysis in terms of the effect of shock Mach number should be generally valid.

Estimated Shock Tunnel Performance

Rather than rely on the perfect gas model used as the basis of the preliminary design analysis, the performance of the UTA shock tunnel was estimated by using the CEC76 computer code developed by Gordon and McBride of the NASA Lewis Research Center.[19] This code calculates shock parameters for incident and reflected shocks as a function of assigned shock velocity. The input data consists of the initial driven gas pressure, temperature, and gas composition. The table of results includes pressure, temperature, density, and Mach number ratios across the incident and reflected shocks. The routine can be used to obtain shock tube parameters for equilibrium and frozen conditions. The CEC 76 code calculations were verified by comparison with the data presented in Ref. 20, and detailed results are presented in Ref. 8.

The effect of the initial driven tube pressure is not significant up to shock Mach numbers of about 5. At higher shock Mach numbers, real gas effects became significant. Lower initial pressures tend to increase atom and ion mass fractions for equilibrium reacting gases. The result is a lower temperature ratio because more energy goes into the zero point energy of the products of dissociation rather than into the translational molecular kinetic energy.

The CEC76 code also provides routines for the calculation of isentropic nozzle performance for both equilibrium and frozen composition during the nozzle expansion. The calculations can be performed as a function of either specified pressure ratio or area ratio distributions. Typical results are displayed in Fig. 8. A chemical kinetics analysis of the nozzle flow was performed by Ha, using the GCKP program developed by Bittker and Scullin[21] of NASA-Lewis Research Center. This analysis concluded that equilibrium nozzle flow would probably be attained for test section Mach numbers up to 8 to 10, depending on shock tube stagnation conditions. Beyond that, the flow is expected to be frozen.

A boundary layer analysis was also conducted by Murtugudde using the nozzle boundary layer code developed by Elliot, Bartz, and Silver[22]. These calculations were used to adjust the CEC76 performance

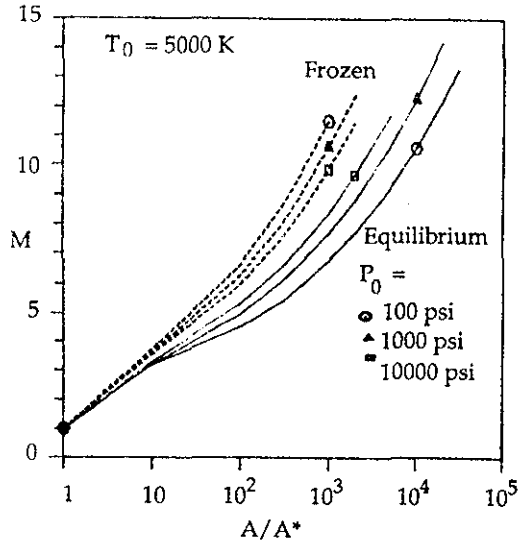

Fig. 8. Mach Number vs Area Ratio

estimates to compensate for nozzle boundary layer growth.

The resulting facility performance map is shown in Fig. 9 in terms of density altitude vs. Mach number. These calculations are based on equilibrium nozzle flow.

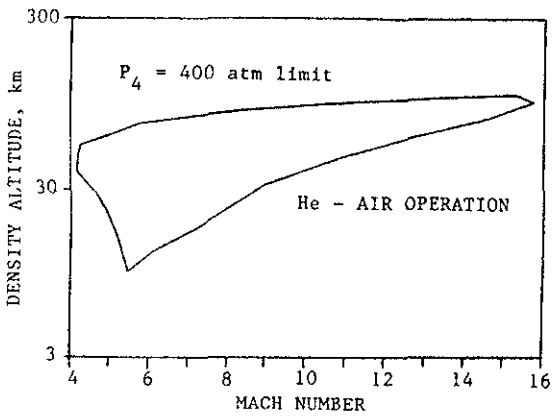

Fig. 9. Hypersonic Shock Tunnel - Density Altitude vs Mach Number

Facility Description

The line diagram of the UTA Hypersonic Shock Tunnel was shown in Fig. 1. A description of the test facility, including the various operational support systems, is given in the following sections. Further details may be found in Ref. 10.

Shock Tube

The shock tube was designed at UTA and constructed in four segments for convenience in transportation after fabrication, installation of instrumentation, and periodic cleaning. The shock tube consists of a single driver tube segment and three driven tube segments. All four segments have been designed for a maximum operating driver pressure of 41.4 MPa (6000 psi) and hydrostatically tested to 62.1 MPa (9000 psi). The driver tube is 3 m (10 ft) long and has an internal diameter of 15.24 cm (6 in) and a wall thickness of 2.54 cm (1.0 in.). One end is closed off with a hemispherical end cap. The other end has a 48.26 cm (19 in) diameter 11.43 cm (4.5 in) thick flange which allows the driver to be bolted to the diaphragm section and driven tube. The various sections of the shock tube are bolted together by 5.08 cm (2 in) diameter bolts. The flanges at each of the section joints are held together by eight of these bolts. The flanges have two O-ring grooves machined in them for sealing purposes. Both high pressure and vacuum seals are obtained by these O-rings. The driven tube is constructed of three segments of 2.74 m (9 ft) length each. All three segments have a flange at each end identical to the one on the driver section. The internal diameter is the same as the driver tube, resulting in a driver to driven tube area ratio of one.

The driver and driven tube are separated by a standard double diaphragm section (Fig. 10).

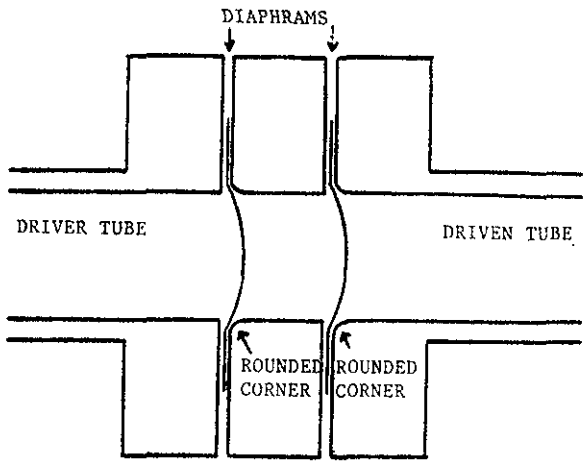

Fig. 10. Double Diaphragm Section

Nozzle, Test Section, and Diffuser

The expansion nozzle, test section, and diffuser were developed by the LTV Aerospace and Defense Company as part of an arc-driven hypervelocity wind tunnel[23] and subsequently donated to UTA. A specially built flange is bolted to the end of the driven tube that mates with a quick disconnect nut on the end of the nozzle to speed replacement of the secondary diaphragm. The nozzle has interchangeable throat inserts (Fig. 11) to provide a variable test section Mach number capability over a range of 5 to 16. The nozzle employs a conical design with a 7.50 degree half-angle expansion. The nozzle has a length of 2.57 m (101 in), with an exit diameter of 33.6 cm (13.25 in) at the test

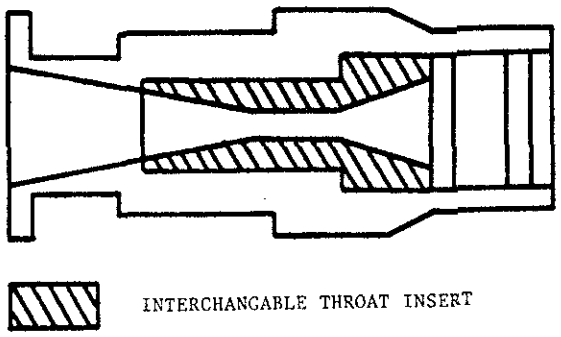

Fig. 11. Nozzle Throat Region

section. The wall of the nozzle contains seven static pressure ports for mounting transducers.

The test section is a semi-free jet design with two access ports on either side. These access ports are 23 cm (9 in) in diameter and can be used for optical windows if desired. The test section housing is 53.6 cm (21.1 in) in length and 44 cm (17.5 in) in diameter. In addition to a portion of the nozzle, the test section housing also contains a conical converging section which leads into the diffuser. This converging section is 38.1 cm (15 in) in diameter in the test section and contracts to a diameter of 31 cm (12.2 in) at the entrance to the diffuser. The converging section captures the flow and generates the first shock wave required to slow the flow down in the diffuser.

The diffuser is a 30.5 cm (12 in) diameter schedule 40 aluminum pipe 213 cm (84 in) long. Near the test section, the aluminum pipe is surrounded by a steel shell with two heavy ports for mounting stings, models, or other equipment in the test section. Two additional ports are provided for routing instrumentation wiring and tubing out of the tunnel. This steel shell is sealed to the aluminum pipe by an O-ring at each end. The other end of the diffuser pipe extends downstream from the the test section, and slides into a slightly larger pipe connected to the vacuum tank. The inner aluminum pipe is allowed to slide inside the other to allow for changes in length of the tunnel and for changing the secondary diaphragm. An O-ring is used to provide the seal between the two pipes.

A second Mach 8 contoured nozzle and associated test section and diffuser assembly is also available. The Mach 8 nozzle has an exit diameter of 20 cm (7.85 in).

Vacuum Tank

The flow exiting the diffuser dumps into a vacuum tank that has a volume of 4.25 m^3 (150 ft^3). A 35.6 cm (14 in) vacuum pipe is connected directly to the tank by a flange joint with a double O-ring seal. This pipe extends inside the building and contains the diffuser pipe described above. A smaller 7.62 cm (3 in) diameter flange is used for connecting the vacuum piping to the vacuum tank. A 1.25 cm (.50 in) pipe collar was also installed during manufacture for hydrostatic proof testing and it is now used for a safety relief valve and a manual vent valve. The vacuum tank was designed for a pressure rating of 103 kPa (15 psi) vacuum and 551 kPa (80 psi) internal pressure. It has been proof tested to an internal pressure of 827 kPa (120 psi).

Pneumatic System

The pneumatic system consists of a high pressure system to pressurize the driver tube and a low pressure system to operate the remote control valves and the booster pump on the high pressure system. Fig. 12 is a schematic of the pneumatic system. The remote control valves are opened by applying air at up to 1.2 MPa (175 psi) to them. A three-way solenoid valve is used to apply this 1.2 MPa (175 psi) air to the valve to open it or vent the line to allow a spring to close the valve. The solenoid valves are operated by electrical power at 24 volts DC with switches located in the control room.

The low pressure system is driven by dry air at 1.2 MPa (175 psi). Regulators are used to reduce the pressure to 689.5 kPa (100 psi) to operate the remote control valves on the high pressure system and to 482.6 kPa (70 psi) to operate the remote control valves which isolate the vacuum transducers. Both vacuum pump isolation valves are operated using 1.2 MPa (175 psi) air. The booster pump in the high pressure system is driven by 1.2 MPa (175 psi) air. A manual valve is located on the control board to allow shutoff of the 1.2 MPa (175 psi) air to the entire system.

The high pressure system can be charged with dry air at up to 14.5 MPa (2100 psi) from a Clark CMB-6 5-stage compressor located in an adjacent compressor building [24] or helium at up to 15.5 MPa (2250 psi) from bottles. A Haskel Model 55696 two-stage booster pump is used to obtain pressures of up to 41.4 MPa (6000 psi) in the driver tube. The booster pump uses filtered compressed air at 689.5 kPa (100 psi) for operation in boosting air or helium to pressures of up to 41.4 MPa (6000 psi). Helium can be stored in a one meter diameter spherical storage vessel at up to 31.0 MPa (4500 psi). This minimizes time to pump up using 15.5 MPa (2250 psi) helium bottles and storage problems associated with the bottles.

Manual valves are located on the control board on the high pressure air and helium supply lines. Manual valves are also located on the booster pump to shut off the supply and control the flow of air to the sphere or driver tube. After the manual valves are set, the high pressure gas system can be operated from the control room by use of remote control valves. These remote control valves are used to isolate the spherical storage vessel, fill the driver tube and diaphragm section, and vent the driver tube and diaphragm section. Safety relief valves for the storage vessel, driver tube, and diaphragm section are also located on the control board.

Vacuum System

The vacuum system consists of two vacuum pumps, two vacuum transducers, and the appropriate piping and valves. The layout of the vacuum system is shown in Fig. 13. The secondary diaphragm separates

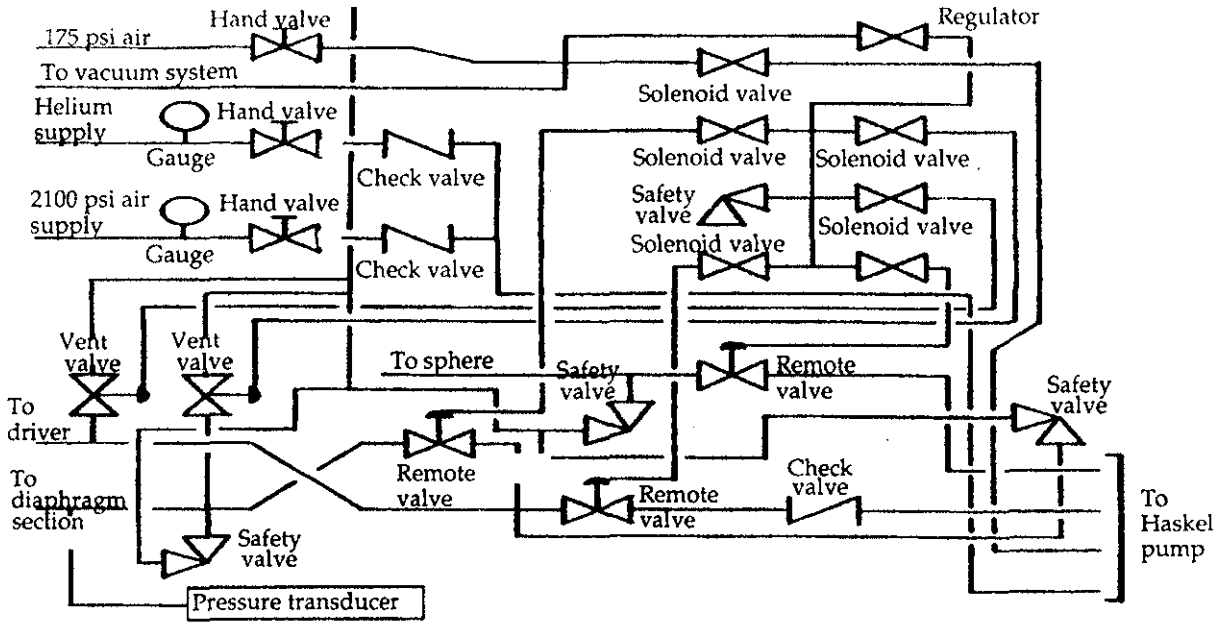

Fig. 12. Pneumatic System Schematic

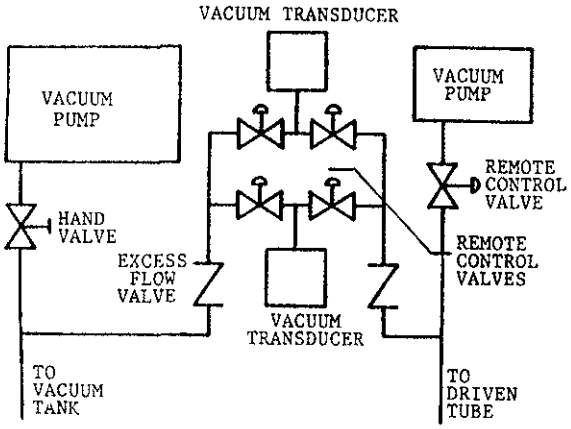

Fig. 13. Vacuum System Schematic

the driven tube region from the nozzle test section, diffuser, and vacuum tank region. Each of these two regions has its own vacuum pump. The driven tube is connected to a Sargent-Welch Model 1376 vacuum pump, which has a free-air displacement of 300 liters per minute and is capable of pumping down to 0.001 mmHg. Stainless steel tubing of 2.54 cm (1.0 in) diameter with compression fittings is used to connect the vacuum pump to the driven tube. The vacuum pump can be isolated by a remotely controlled 2.54 cm (1.0 in) diameter ball valve to protect it from the high pressure in the driver tube.

The vacuum tank is connected to a Sargent-Welch Model 1396 vacuum pump which has a free-air displacement of 2800 liters per minute and is capable of pumping down to 0.0001 mmHg. The vacuum pump is connected to the vacuum tank by 7.62 cm (3 in) diameter threaded schedule 40 black pipe. A valve is also included in the vacuum line to isolate this vacuum pump as well.

Pressure is measured in the driven tube and vacuum tank by two MKS Baratron Type 127A pressure gauges. One gauge has a full-scale range of 1000 mmHg and an accuracy of 0.1 mmHg while the other has a full-scale range of 10 mmHg and an accuracy of 0.001 mmHg. Both gauges are protected against overpressure damage to 241.3 kPa (35 psi). Each gauge can be connected to measure the pressure in either the driven tube or the vacuum tank by remotely operated valves. Each gauge is also protected against overpressure by a Nupro Excess Flow valve. These valves will protect the gauges should the remote control valves not be closed prior to a run, or if the primary diaphragms rupture prematurely.

Electrical Control System

The electrical control system consists of the coils on the solenoid valves, a transformer to power the coils, a power supply and display for the vacuum transducers, displays for the driver, diaphragm, and driven tube pressures and driver tube temperature switches to control the solenoid valves, and the wiring to connect the system together. Fig. 14 shows the schematic of the electrical control system and Fig. 15 shows the schematic of the electrical display system.

All the displays and switches are mounted on panels in the control room. The transformer to power the solenoid valves is mounted in the control room behind

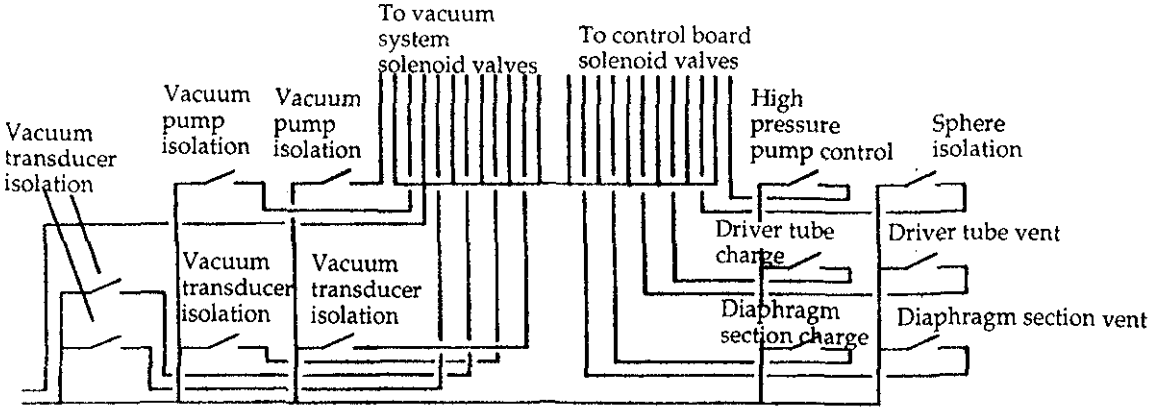

Fig. 14. Electrical Control System Schematic

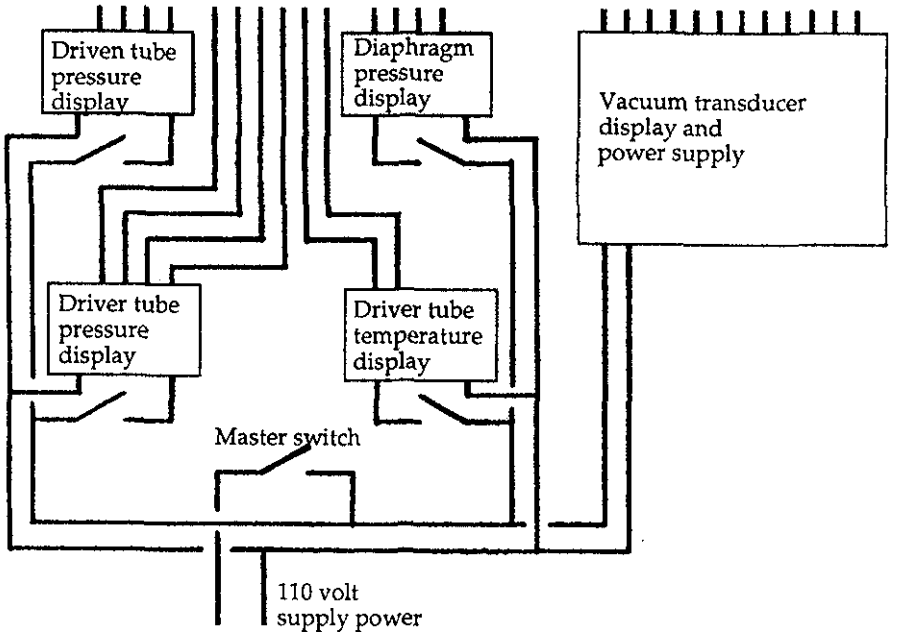

Fig. 15. Electrical Display System Schematic

the panels. Power switches for the displays and a master power switch are also provided.

Instrumentation

The hypersonic shock tunnel is currently instrumented with several different types of pressure transducers and thermocouples. In addition to the MKS capacitance transducers in the vacuum system, other instrumentation includes Kulite pressure transducers, Medtherm thermocouples, and PCB Piezotronic dynamic quartz transducers. The driver tube is instrumented with a Kulite model XTM-190-5000A pressure transducer and a Medtherm model TCS-103-J type J thermocouple. The pressure transducer is rated at 34.5 MPa (5000 psi) and is protected against overpressure damage up to 41.4 MPa (6000 psi). The driven tube is instrumented with six Kulite model XTS-190-300A pressure transducers rated for 2.07 MPa (300 psi) with an overpressure rating of 4.14 MPa (600 psi). Thermocouples are located at the same locations along the tube. The thermocouples are model TCS-103-J as well. All the Kulite pressure transducers are powered by a 10 volt regulated power supply.

Stagnation temperature and pressure behind the reflected shock wave at the end of the driven tube are measured by a Medtherm model TCS-103-E thermocouple and a PCB Piezotronic model 134A dynamic pressure transducer with a full scale pressure rating of 68.9 MPa (10,000 psi). This transducer has a

resolution of 6.89 kPa (1.0 psi) and a rise time of 0.2 microseconds.

The expansion nozzle attached to the end of the driven tube is instrumented with seven PCB Piezotronic model 103A02 pressure transducers. These transducers have a sensitivity of 0.29 mV/Pa (2000 mV/psi), a resolution of 0.172 Pa (2.2×10^{-5} psi), a useful range from -14.8 to +41.4 kPa (-2 to +6 psi), and a maximum allowable pressure of 206.8 kPa (30 psi). All the PCB Piezotronic transducers are driven by a special power supply signal conditioner which uses the same pair of wires to each transducer for both power and signals. The transducers use 24 volt DC at 4 milliamps for operation at a gain of one.

Data Acquisition System

The data acquisition system is a LeCroy system currently capable of recording up to 40 channels of data. Data is recorded by three different modules. The power supply for the high pressure transducers is also located in the data system crate. This allows the excitation voltage to the transducer and the signal voltage from the transducer to the data acquisition system to be combined into one cable assembly.

Eight high-speed data acquisition channels are recorded by two LeCroy model 6810 waveform recorders. Each module can be programmed to record 1, 2, or 4 channels at speeds of up to 5 Msamples/sec depending upon the number of channels used. An external clock may also be used for sampling rate timing. Other parameters which can be programmed include input signal coupling, full scale voltage, and offset voltage. Each of the 6810 modules contain 512 k of memory for data storage which may be used among the active channels.

The remaining lower-speed 32 channels are monitored by a LeCroy model 8212A data logger. The number of active channels is programmable from 4 to 32. Data from the 8212A is stored in a model 8800A memory module connected to the 8212A by a ribbon cable. The memory module has 32 k of memory which is automatically divided equally among the active channels. The sampling rate can be varied between 40 kHz and 0.2 kHz depending upon the number of active channels. Slower sampling rates can be obtained by using an external clock.

Triggering the system is accomplished by using the PCB quartz transducer output as the trigger signal. This signal was fed into one of the 6810 modules as an external trigger. This module acted as a master controller by generating a synchronized signal to trigger the other 6810 module and the 8212A module. Triggering can also be accomplished by using input channel 1 or 2 of a 6810 as a source. The external trigger voltage level can be set to values between -5 and +5 volts. A delay can also be used to allow data to be collected after a predetermined elapsed time. This can also be used to record data before the trigger signal is received since data is constantly being taken and written over previous data in memory once the system is armed. The trigger signal causes the system to mark the location and collect enough data to fill the memory allocation once more but not write over the desired data.

Data is transferred to the host computer by a General Purpose Interface Bus (GPIB) interface. A LeCroy model 8901A module is used to connect the data acquisition system with the GPIB bus. The cable length is severely limited by the GPIB interface. The problem is overcome by the use of bus extenders which allow the data acquisition system to be located beside the hypersonic shock tunnel and the computer in the control room. Figure 16 is a schematic of the computer and data system layout.

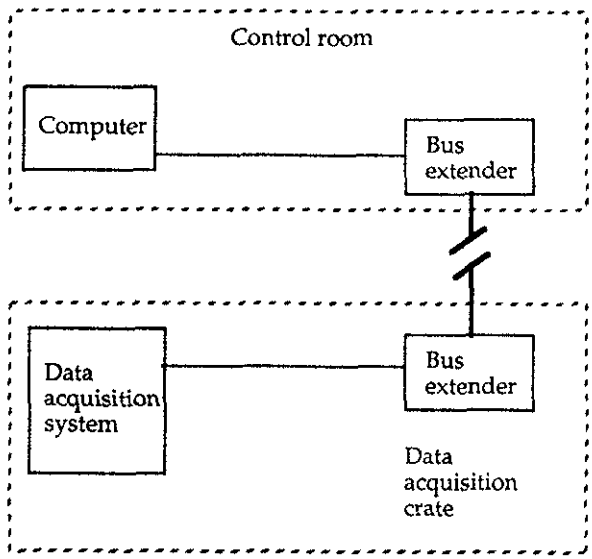

Fig. 16. Computer and Data System Block Diagram

Experimental Test Program

Facility Checkout

The initial operation of the tunnel consisted of a number of test runs at increasing pressure levels to verify the design and refine the operational procedures. The first series of test runs employed mylar diaphragms, and the data acquisition system was triggered by taping a thin strip of aluminum foil to the mylar that was broken by the rupture of the diaphragm. The aluminum foil was connected to a power supply in the data acquisition trigger circuit, and when broken, allowed the voltage to be applied to the trigger. At higher pressure levels, the use of steel diaphragms was required, and the output signal from the PCB quartz transducer used to measure the pressure at the end of the driven tube was used to trigger the data acquisition system.

Diaphragm Development

Driver pressures greater than 3.45 MPa (500 psi) were obtained by using steel diaphragms. Several

diaphragms were tested to determine the pressure obtainable for various diaphragm thicknesses. The initial steel diaphragms were made from 0.51 mm (0.020 in) thick type 1010 steel shim stock. The entire diaphragm was blown downstream with no evidence of petaling. The first run with a double diaphragm configuration provided a driver pressure of 2.76 MPa (400 psi) before rupture. Both diaphragms were scored to a depth of 0.13 mm (0.005 in). After this run it was obvious that much thicker steel would be required, so three new thicknesses of 1.21 mm (0.0478 in or 18 Ga.), 1.90 mm (0.0747 in or 14 Ga.), and 2.66 mm (0.1046 in or 12 Ga.) were tried. Although only three different diaphragm thicknesses were examined, a wide variation of rupture pressure level could be obtained by varying the scoring depth. The scoring pattern creates four petals when the diaphragm bursts and is shown in Fig. 17. The scoring is done with a conical burr tool to

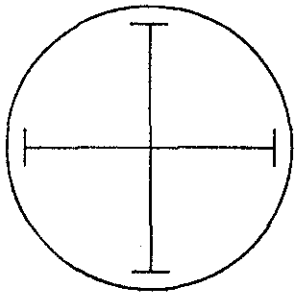

Fig. 17. Diaphragm Scoring Pattern

produce a stress concentration along a fine line. The diaphragm thickness at these grooves is referred to as the effective thickness. The ratio of effective thickness to original diaphragm material thickness did not appear to be a key parameter, although there is probably a practical lower limit. The diaphragms worked well as long as the scoring depth was at least 0.38 mm (0.015 in). Thicker diaphragm material probably will require deeper scoring for good results. The bursting pressure for various scoring depths of the three material thicknesses is shown in Table 1. Figure 18 shows the effective thickness required for a given pressure differential.

Shock Tube Performance

Figure 19 shows four pressure traces along the length of the driven tube for a typical run. This figure illustrates the passage of both the incident and reflected shock waves. The pressure level created by the incident shock wave is constant for a short time before beginning to slowly rise again. This gradual pressure rise is due to the passing of the tail of the expansion wave created by the diaphragm rupture. The tail of the expansion wave travelled down the driven tube since the flow behind the incident shock wave was supersonic. As the incident shock Mach number

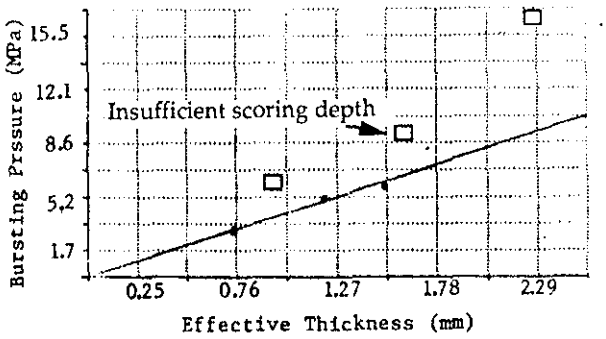

Fig. 18. Diaphragm Bursting Pressure as a Function of Effective Thickness

Table 1. Diaphragm Bursting Pressure as a Function of Material Thickness and Scoring Depth

Scoring Depth (mm)	18 Gauge	14 Gauge	12 Gauge
0.279	6.205 MPa		
0.457	3.103 MPa		
0.279		9.239 MPa	
0.686		5.033 MPa	
0.381			16.548 MPa
1.143			5.792 MPa
1.905			2.896 MPa

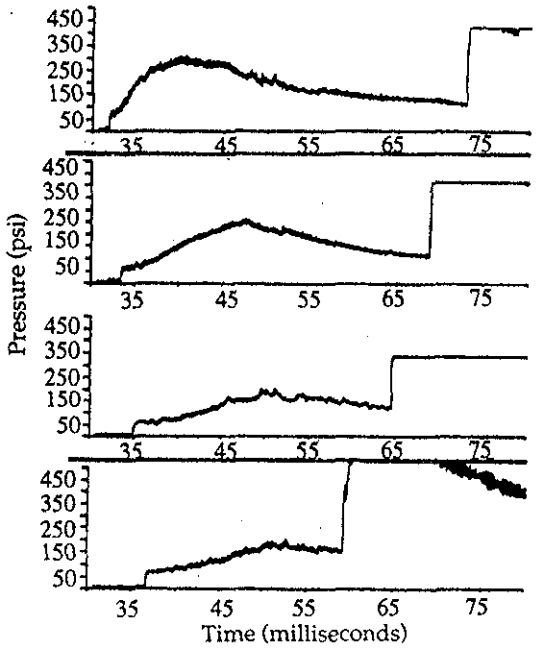

Fig. 19. Sample Shock Tube Time Traces

increased from case to case, the time between the arrival of the shock wave and the arrival of the expansion wave decreased, as expected.

The reflected shock wave increased the pressure to a higher level than the incident shock did. This was expected and observed from the measurements. The pressure behind the reflected shock wave at the end of the driven tube is the stagnation pressure for the nozzle expansion. A direct measurement of the average shock speed (both incident and reflected) can be obtained by measuring the time interval between shock passage detected by these pressure transducers. This data for the incident shock is shown in Table 2 for a typical case, and compares favorably with ideal gas predictions of shock speed. The reflected shock speed calculated by the time required to travel between instrumentation locations increased with time and distance. This was not expected at all, but was observed consistently. The reflected shock wave encounters a continually decreasing local pressure at it travels back up the driven tube. The decreasing pressure is a result of the expansion wave. The pressure traces show the decreasing pressure just before the passage of the reflected shock wave. The reflected shock wave must speed up to maintain a constant pressure after the reflected shock wave.

A complete summary of the comparison between theory and experiment for a typical case is shown in Table 2. The ideal gas theory was summarized earlier, and provides a direct method of calculating shock speed, U_s, pressure behind the incident shock, P_2, and reflected shock, P_5 as a function of P_4/P_1. The values in the column labeled CEC76 were calculated from the CEC76 code as a function of measured shock speed. The calculated pressures were greater than the measured value for both methods. Consideration of the boundary layer growth and its effect on shock attenuation leads one to expect the shock wave would slow down as it travelled down the driven tube. The slower shock speed would also reduce the pressure rise across the shock wave. The pressure rise calculated by the CEC76 computer code was lower than the rise calculated by ideal gas normal shock relations. The measured initial pressure rise behind the incident shock wave is lower than predicted by both methods but within the expected range considering the effects of shock wave attenuation due to the boundary layer growth. The large discrepancy between the calculated and measured values for the stagnation pressure P_5 (Station 7) may be due to the use of this transducer as the triggering signal for the data acquisition system in addition to its use for pressure measurement. For this reason, the value of P_5 from the CEC76 calculations based on measured shock speed was used as the stagnation pressure for the nozzle expansion. Data from other tests show similar trends, and are discussed in more detail in Ref. 10.

Table 2. Shock Tube Performance Comparison Between Theory and Experiment

Item	Theory (Ideal Gas)	Theory (CEC76)	Exp. Date	
P_4			10.45 MPa	
P_1			34.5 KPa	
P_4/P_1			303	
P_{ts}			1.62 KPa	
U_s	954.3		STA	U_s, m/s
			1-2	952.5
			2-3	941.5
			3-4	924.8
P_2	298.5 KPa	284.8 KPa	STA	P_2,KPa
			1	289.6
			2	262.0
			3	234.4
			4	248.2
			7	193.1
P_5	1.63 MPa	1.60 MPa	STA	P_5,KPa
			7	0.772

Nozzle Performance

The nozzle configuration tested was designed to produce a test section Mach number of eight. the nozzle pressure data obtained verified that the nozzle started for the test cases considered. The quality of the flow in the test section was not determined since a pitot rake was not yet available for total pressure measurements. The thickness of the boundary layer could not be determined precisely, for the same reason.

A typical nozzle static pressure vs time trace is shown in Fig. 20. The starting shock and expansion wave system is clearly observed, followed by a steady-flow test period of 3-4 msec duration. This is followed by a second period of slightly higher pressure of about 10 msec duration. This is thought to be the flow corresponding to the 'equilibrium mode', however verification of this will require detailed total pressure and temperature rake measurements. The third relatively longer period of steady flow probably corresponds to the "blow-down" period of tunnel operation.

The nozzle performance is summarized in the form of pressure ratio vs area ratio for a typical case Ms = 2.75) in Fig. 21. The isentropic flow calculations are shown for comparison, and indicate the existence of a relatively thick nozzle boundary layer, as expected. Nozzle flow calculations obtained with the aid of the boundary layer code developed by Elliot, Bartz and Silver[22] are also shown for comparison, and agree reasonably well with the experimental data.

Concluding Remarks

The hypersonic shock tunnel developed at UTA provides a unique capability for faculty and graduate student research in hypersonic aerodynamics. Initial operational results have verified the design concept. Additional calibration studies will include a detailed total pressure rake survey of the nozzle flow and

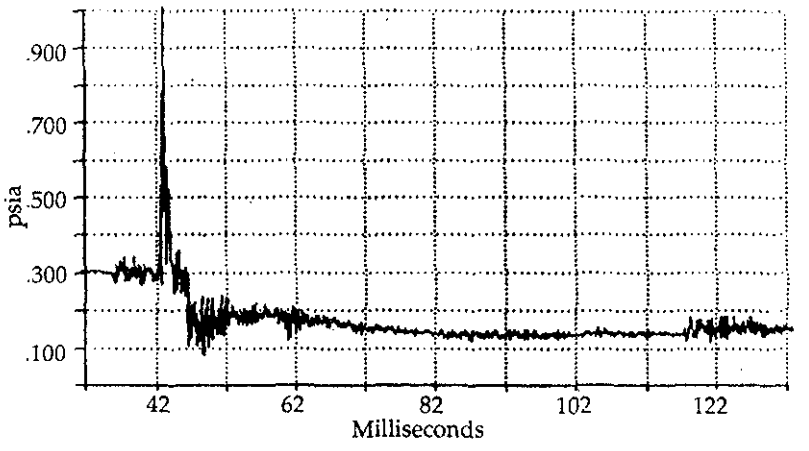

Fig. 20. Typical Nozzle Pressure Trace, $M_S = 2.75$

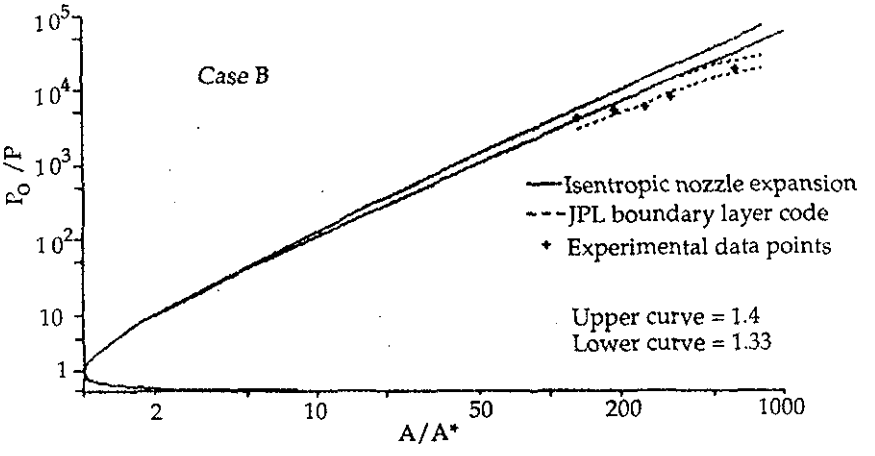

Fig. 21. Nozzle Performance, $M_S = 2.75$

verification of the total enthalpy level estimated from the real gas shock tube calculations with calculations of total enthalpy based on stagnation point heat transfer measurements coupled with the Fay-Riddell Theory.[25] Extensions of the calibrated performance map to higher shock Mach numbers and an extended range of test section Mach numbers are planned for the near future.

References

1. Resler, E.L.,Lin, S.C., and Kantrowitz, A., "The Production of High Temperature Gases in Shock Tubes," J. Appl. Phys. Vol. 23, 1952.
2. Lukasiewicz, J., "Shock Tube Theory and Applications," N.R.C. Report MT-10, Ottawa, Canada 1950.
3. Glass, I.I., and Hall, J., "Handbook of Supersonic Aerodynamics," Section 18 "Shock Tubes," NAVORD Report 1488, Vol. 6, 1957.
4. Bradley, J., Shock Waves in Chemistry and Physics, John Wiley and Sons, New York, 1962.
5. Hertzberg, A., Wittliff, C.E., and Hall, J.G., "Development of the Shock Tunnel and its Application to Hypersonic Flight," Progress in Astronautics and Rocketry, Volume 7, 1962.
6. Anon., "A Catalogue of European Hypersonic Wind Tunnel Facilities," AGARD Report No. 619, 1975.
7. Penaranda, F.E., and Freda, M.S., "Aeronautical Facilities Catalogue, Vol. 1 - Wind Tunnels," NASA RP-1132, January 1985.
8. Murtugudde, R.G., "Hypersonic Shock Tunnel," M.S. Thesis, The University of Texas at Arlington, May 1986.
9. Ha, Q.M., "Flow of Nonequilibrium Chemically Reacting Gas Mixture in a Hypersonic Nozzle," M.S. Thesis, The University of Texas at Arlington, May 1987.

10. Stuessy, W.S., "Hypersonic Shock Tunnel Development and Calibration," M.S. Thesis, The University of Texas at Arlington, December 1989.

11. Anderson, J.D., Jr., Modern Compressible Flow, McGraw Hill Book Company, New York, 1982.
12. Angelone, J.P., "Shock Tube - High Temperature Gas Dynamic Studies," M.S. Thesis, The University of Texas at Arlington, May 1978.
13. Wittliff, C.E., Wilson, M.R., and Hertzberg, A., "The Tailored-Interface Hypersonic Shock Tunnel," J. Aero. Sc., Vol. 26, No. 4, April 1959.
14. Holder, D.W. and Schultz, D.L., "The Duration and Properties of the Flow in a Hypersonic Shock Tunnel," Progress in Astronautics and Rocketry, Vol. 7, 1963.
15. Smith, C.E., "The Starting Process in a Hypersonic Nozzle," J. Fluid Mech., Vol. 24, Part 4, April 1966.
16. Amann, H.O., and Reichenbach, H., "Unsteady Flow Phenomenon in Shock Tube Nozzles," Proceedings of the Ninth International Shock Tube Symposium, Stanford Univ., 1973.
17. Huang, S.J., "A Study of Flow in Shock Tubes," M.S. Thesis, The University of Texas at Arlington, December 1988.
18. Mirels, H., "Shock Tube Test Time Limitation due to Turbulent Wall Boundary Layer," AIAA J., Vol. 2, No. 1, Jan. 1964.
19. Gordon, S., and McBride, B.J., "Computer Program for Calculation of Complex Chemical Equilibrium Compositions, Rocket Performance, Incident and Reflected Shocks, and Chapman-Jouget Detonations," NASA SP 273, 1971.
20. Feldman, S., "Hypersonic Gas Dynamic Charts for Equilibrium Air," AVCO Research Report NO. 40, 1957.
21. Bittker, D.A., and Scullin, V. J., "General Chemical Kinetics Computer Program for Static and Flow Reactions, with Application to Combustion and Shock-Tube Kinetics," NASA TN D-6586, 1972.
22. Elliott, D.G., Bartz, D.R., and Silver, S., "Calculation of Turbulent Boundary-Layer Growth and Heat Transfer in Axi-Symmetric Nozzles," JPL TR No. 32-382, 1963.
23. Stalmach, C.J., Jr., "Design and Operation of a Variable-Volume Arc Chamber in a Hypervelocity Wind Tunnel," Proceedings of the 4th Hypervelocity Techniques Symposium, Arnold Engineering Development Center, Tennessee, 1965.
24. Wilson, D.R., "Development of the University of Texas at Arlington Aerodynamics Research Center," AIAA Paper 88-2002, AIAA 15th Aerodynamic Testing Conference, San Diego, Ca., May 18-20, 1988.
25. Fay, J.A., and Riddell, F.R., "Theory of Stagnation Point Heat Transfer in Dissociated Air," J. Aero. Sc., Vol. 25, 1958.